ARTICLES
https://doi.org/10.1038/s41929-022-00823-1

nature catalysis

Check for updates

Site-selective proteolytic cleavage of plant viruses by photoactive chiral nanoparticles

Rui Gao[1,2,13], Liguang Xu[1,2,3,13], Maozhong Sun[1,2,13], Manlin Xu[4,13], Changlong Hao[1,2], Xiao Guo[1,2], Felippe Mariano Colombari[5], Xin Zheng[6], Petr Král[6], André F. de Moura[7], Chuanlai Xu[1,2] ✉, Jinguang Yang[8] ✉, Nicholas A. Kotov[9,10,11] ✉ and Hua Kuang[1,2,12] ✉

Viral diseases of plants are associated with large health and economic costs. Antiviral agents developed for mammalian organisms have had limited success for plants, necessitating alternative strategies to address this biological and sustainability problem. Here we show that chiral 3 nm $Cu_{1.96}S$ nanoparticles can site-selectively cleave capsid in tobacco mosaic virus under sunlight. With D-penicillamine as surface ligands, the nanoparticles display high affinity to the Gln 99 to Ala 105 segment in the capsid via a network of supramolecular bonds and 3,000–10,000 times lower affinity to capsids of other viruses. Illumination with green light leads to polarization-dependent, protease-like hydrolysis of the amide bond between Asn 101 and Pro 102. Nanoparticles inhibited viral infectivity by 98.7% in protoplasts and 92.6% in plants while avoiding hypersensitive response and large environmental impact. These findings show that nanoparticles combining proteolytic activity due to metal ions and site selectivity due to nanoscale chirality can be used as effective antiviral agents.

Annual loss of crops due to viral infections of plants exceeds 20% and continues to rise[1,2]. Antiviral pesticides[3,4], similar to those used for blocking viruses in mammalian organisms, can also prevent vegetal infections but require multiple doses due to their photosensitivity[5,6]. Gene engineering protocols using a variety of techniques[7–9] can also be implemented but low translatability of the genes imparting resistance to plant viruses combined with high rates of viral escape and transfer between different plant families have hampered the development of transgenic plants with viral resistance[10]. These challenges necessitate chemical approaches to address viral threats for plants and other food supplies that are becoming more urgent as the Earth's population grows[11].

Organic and inorganic nanostructures developed for humans can potentially be used to suppress plant viruses by delivering genetic or chemical agents[12–21]. While realistic for some agricultural enterprises, the high cost, environmental degradation and large losses of expensive biopolymers, nanomaterials and genetic constructs pose difficult economic thresholds especially for crops with the highest rates of plant disease and communities with food supply vulnerability[22]. Environmentally robust inorganic biomimetic nanoparticles (NPs), engineered to serve as antiviral agents[23], are an alternative pathway to inhibit or destroy viruses[24–26]. However, nanoscale materials with antiviral activity are known to be non-selective and toxic[27], a primary example being silver NPs causing broad spectrum toxicity for the host. Minimally decorated NPs from Earth-abundant elements that selectively adhere to and destroy specific viruses are necessary to avoid indiscriminate antiviral action in the plant microbiome, mitigate the toxicity and reduce the cumulative environmental impact of pesticides. The fundamental and practical significance of finding a path to engineer such NPs is very important in the context of capsid-targeted viral inactivation.

There is a specific chiral recognition effect between chiral substances[28,29]. We hypothesized that imparting chirality to metal–sulfide or metal–oxide NPs could improve their biological targeting[30–33] and other functionalities such as their optical activity[34]. To test this hypothesis we chose one of the best-known agricultural threats, tobacco mosaic virus (TMV)[35], which can reduce the harvest of tomatoes, potatoes, peppers and other plants from the *Solanaceae* family by 30%[36]. TMV also infects beans, cucumbers, grapes and apples. The capsid of TMV exhibits highly ordered helical arrangement, and its RNA is embedded in the helical arrangement of the capsid, resulting in the virus featuring open-ended geometry and an inner rod-like cavity of 4 nm (ref. [37]). This makes it possible for NPs to be accommodated within the cavity by adjusting their size and surface chirality. Although not likely to be sufficient, the geometric complementarity of the nanoscale dimensions of the viral host and the NP guest can contribute to selectivity during their interaction. Previous studies[38,39] indicated that circular polarization of incident photons may affect the photoreactions between chiral NPs and proteins. Thus, in this work, we showed that chiral 3 nm $Cu_{1.96}S$ NPs can selectively cleave the capsid of TMV under circularly polarized light (CPL). Chiral NPs with D-penicillamine as the surface ligand show high affinity for the Gln 99 to Ala 105 fragment in the TMV capsid. The amide bond between Asn 101 and Pro 102 in the TMV capsid can thus be hydrolysed by chiral NPs in a polarization-dependent way when irradiated with light at 532 nm. We thoroughly elucidated

[1]State Key Laboratory of Food Science and Technology, Jiangnan University, Wuxi, China. [2]International Joint Research Laboratory for Biointerface and Biodetection, Jiangnan University, Wuxi, China. [3]The Key Laboratory of Synthetic and Biological Colloids, Ministry of Education, School of Chemical and Material Engineering, Jiangnan University, Wuxi, China. [4]Shandong Peanut Research Institute, Qingdao, China. [5]Brazilian Biorenewables National Laboratory (LNBR), Brazilian Center for Research in Energy and Materials (CNPEM), Campinas, Brazil. [6]Department of Chemistry, University of Illinois at Chicago, Chicago, IL, USA. [7]Department of Chemistry, Federal University of São Carlos, São Carlos, Brazil. [8]Tobacco Research Institute of Chinese Academy of Agricultural Sciences, Qingdao, China. [9]Department of Chemical Engineering, University of Michigan, Ann Arbor, MI, USA. [10]Biointerfaces Institute, University of Michigan, Ann Arbor, MI, USA. [11]Michigan Institute for Translational Nanotechnology, Ypsilanti, MI, USA. [12]Science Center for Future Foods, Jiangnan University, Wuxi, China. [13]These authors contributed equally: Rui Gao, Liguang Xu, Maozhong Sun, Manlin Xu. ✉e-mail: xcl@jiangnan.edu.cn; yangjinguang@caas.cn; kotov@umich.edu; kuangh@jiangnan.edu.cn

the chemical mechanisms of affinity and the hydrolysis reaction, and then applied chiral NPs to inhibit viral infection, achieving high inhibition rates of 98.7% and 92.6% in protoplasts and plants, respectively, which occurred without allergic reactions or large environmental impact. These findings suggest that site-selective NPs incorporating metal-ion-based proteolytic activity and nanoscale chirality can be used as potent antiviral agents.

Results

Preparation and characterization of antiviral chiral NPs. We synthesized copper sulfide NPs with a diameter of 3 ± 0.5 nm (Fig. 1), stabilized by penicillamine (Pen), by modifying previously developed protocols[40,41] (Fig. 1a). The NPs will be denoted as D-NPs, L-NPs and rac-NPs when D-, L- and rac-Pen were used as surface ligands, respectively. Having slightly oblong geometry, NPs carrying L- and D-Pen had nearly the same diameter, shape and size distribution (Fig. 1b,d,f). The lattice spacings of 0.285 nm and 0.33 nm observed in the transmission electron microscopy (TEM) images of NPs corresponded to the (200) and (311) lattice planes of monoclinic $Cu_{1.96}S$ crystal, respectively (Fig. 1c,e). X-ray diffraction and other spectral data (Supplementary Fig. 1) were consistent with $Cu_{1.96}S$ in a monoclinic crystal lattice (Fig. 1g). X-ray photoelectron spectra (XPS) showed two strong Cu 2*p* peaks assigned to Cu^{+} and Cu^{2+}, confirming the X-ray diffraction results. The deconvolution of the S 2*p* XPS spectra produced two doublets that were assigned to Cu–S and S–S in the inorganic core of the NPs. Electronic binding energies for nitrogen and oxygen did not obviously change versus free Pen (Supplementary Fig. 2). The intensity of the peak corresponding to the sulfhydryl –S–H groups was obviously reduced, and the peak representing hydrogen bonds increased compared with Pen in the Fourier-transform infrared (FT-IR) spectra (Fig. 1h). This indicated that the ligand was bound to the NP surface via a strong S–Cu covalent bond and a weak S–H–O hydrogen bond.

The D-NPs and L-NPs exhibited circular dichroism (CD) peaks at 301, 412, 560 and 790 nm (Fig. 1i) with optical asymmetry *g*-factors of 0.25 ± 0.01 at 918 nm, 0.05 ± 0.002 at 600 nm and 0.01 ± 0.0004 at 450 nm (Supplementary Fig. 2). The number of Pen molecules on the surface of the D-NPs was ~150, as determined by liquid chromatography–mass spectrometry (LC–MS) and thermogravimetric analysis (Supplementary Fig. 3).

Light-induced cleavage of TMV capsid. The constitutive units of the capsid protein (CP) are CP monomers; they are composed of 158 amino acids and have a molecular weight of 17.5 kDa. The self-assembly of 2,130 CP monomers produces the tube-shaped capsid of the complete virus[35]. Capsid protein rings (CPRs) are self-assembled from 49 CP monomers. These nanoscale protein structures often serve as TMV models in biological studies and are obtained by expressing CP monomers in *Escherichia coli*. (Fig. 1j). The known photocatalytic activity of semiconductor NPs prompted us to investigate the structural changes in the virus particles under light. TMV material extracted from infected tobacco primarily consisting of several CPRs[35] was used to investigate photolytic processes induced by NPs in the viral cavities. We found that the rod-like bodies of the viruses were destroyed and changed into irregular aggregates after 3 days of illumination with simulated unpolarized sunlight in an artificial climate chamber (25 °C temperature, 60% relative humidity, 2,000 lux illuminance) in the presence of D-NPs (Fig. 2a). In the benchmark experiments, TMV capsids were not destroyed when the virus material was treated with chiral NPs or light alone (Supplementary Fig. 4). Besides TEM evidence, western blotting assay (Fig. 2b) showed that the band corresponding to CP faded away after illumination and NP treatment; this indicated that the antiviral activity is dependent on NP concentration and light intensity and confirmed the importance of both factors (Supplementary Fig. 4). Similar evidence of strong proteolytic activity of photoexcited NPs was also observed when TMVs were illuminated in presence of L-NPs, but to a lesser extent, giving an initial indication of chiral preferences for TMV cleavage (Fig. 2c and Supplementary Fig. 4).

Since the strongest CD peak of chiral NPs was observed at 560 nm (Fig. 1i), the illumination source for light polarization effects was a laser emitting at 532 nm. Unlike typical simulated sunlight in the growth chamber, the polarization of the laser illumination can be varied, which was essential for establishing the mechanism of virucidal activity. Negatively stained TEM images, western blotting assay and CD spectra (Fig. 2) were employed to characterize the interactions between chiral NPs and TMV or CPRs under left circularly (LCP), right circularly (RCP) and linearly (LP) polarized light. Illumination of TMVs for 6 h in the presence of D-NPs revealed the maximum activity when RCP was used, and no changes were observed for illumination with LCP (Fig. 2d); such selectivity is quite remarkable from a fundamental standpoint. Based on the western blotting assay (Fig. 2f, g), the efficiencies for virus destruction by D-NPs are 93.8%, 33.7% and 0% when illuminated with RCP, LP and LCP, respectively. When TMV is exposed to L-NPs, the efficiency for virus destruction was 0%, 26.8% and 87.8% for RCP, LP and LCP illumination, respectively (Fig. 2e and Supplementary Fig. 5). For rac-NPs, the efficiency for virus destruction was 0% for all polarizations (Table 1 and Supplementary Fig. 6). The polarization-dependent cleavage of chiral NPs was also verified through illuminating recombinant CPRs for 6 h in the presence of *D*-NPs. Based on the TEM images, western blotting assay and CD spectra (Fig. 2h–k), the efficiency for recombinant CPR decomposition by D-NPs was 98.4%, 61.2% and 0% when being illuminated with RCP, LP and LCP, respectively. When recombinant CPRs were exposed to L-NPs, the efficiency for CPR destruction was 0%, 56.7% and 88.6% when illuminated with RCP, LP and LCP, respectively. CD spectra revealed that the α-helix content sharply decreased while random coil conformation greatly increased after illumination in the presence of NPs (Fig. 2l,m and Supplementary Fig. 6). CPRs remained intact when illuminated in the presence of rac-NPs (Table 1 and Supplementary Figs. 5 and 6).

Considering that sunlight is weakly polarized, our main goal in this part of the study was to understand the mechanism of the photoinduced cleavage and chiral selectivity with respect to L- and D-NPs. Besides being fundamentally intriguing, the process dependence on light polarization may be practically important as a laboratory tool to increase both the efficiency and reproducibility of the viral cleavage, and as a method for virus analysis including those for specific mutations.

Fig. 1 | Synthesis of Pen-modified chiral nanoparticles. a, Schematic illustration of the formation of chiral NPs. Dotted lines represent S–H–O hydrogen bonds between the surface ligands and NPs. $CuCl_2$ is the copper source, Pen is a sulfur source and a surface ligand, and $NaBH_4$ is a reducing agent and pH regulator. **b**,**c**, Representative TEM (**b**) and high-resolution TEM (**c**) images of D-NPs. **d**,**e**, Representative TEM (**d**) and high-resolution TEM (**e**) images of L-NPs. **f**, The size distribution of L-NPs and D-NPs was obtained by dynamic light scattering. Dots represent the experimental light scattering. **g**, The X-ray diffraction patterns of L-NPs and D-NPs and the standard X-ray diffraction patterns for $Cu_{1.96}S$ (PDF#12-0174). **h**, The FT-IR spectra of Pen, D-NPs and L-NPs. The 2,500 cm^{-1} stretch was assigned to mercapto groups. **i**, The CD spectra of L-NPs and D-NPs with and without CPRs in the dark. All the experiments were performed in triplicate. **j**, Schematic illustration of the formation of a CPR and TMV. TMV consists of CP and RNA; RNA is embedded in the CP to form a helical tube with two open ends. The CP is formed by self-assembly of 2,130 CP monomers. RNA (white and blue section) is interweaved with the inner rim of the helical capsid. CPRs are obtained by expressing in *E. coli*, and are self-assembled from 49 CP monomers.

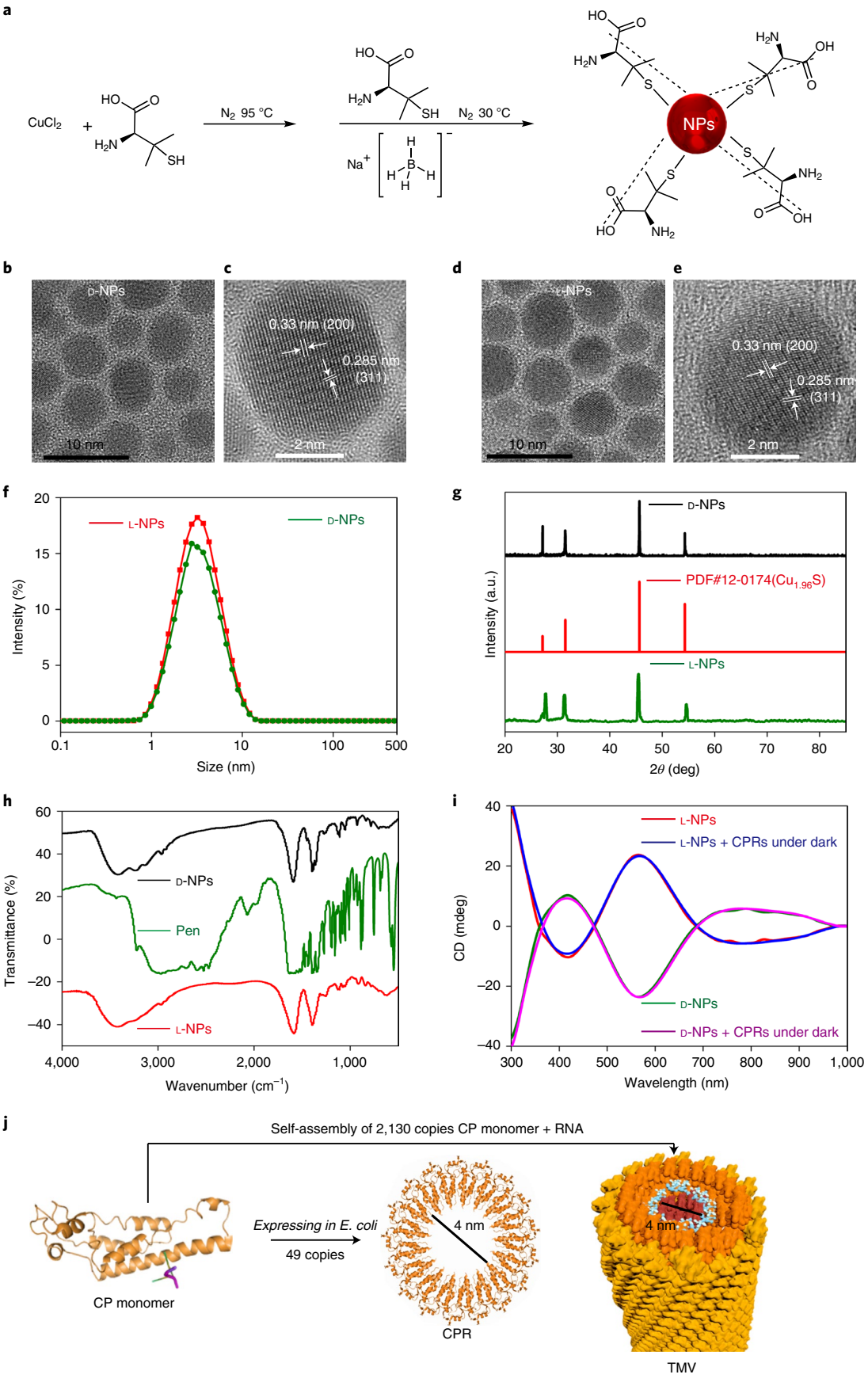
a
CuCl2
N2 95 °C
N2 30 °C
Na+
NPs
b
D-NPs
10 nm
c
0.33 nm (200)
0.285 nm (311)
2 nm
d
L-NPs
10 nm
e
0.33 nm (200)
0.285 nm (311)
2 nm
f
L-NPs
D-NPs
Intensity (%)
Size (nm)
g
D-NPs
PDF#12-0174(Cu1.96S)
L-NPs
Intensity (a.u.)
2θ (deg)
h
D-NPs
Pen
L-NPs
Transmittance (%)
Wavenumber (cm−1)
i
L-NPs
L-NPs + CPRs under dark
D-NPs
D-NPs + CPRs under dark
CD (mdeg)
Wavelength (nm)
j
Self-assembly of 2,130 copies CP monomer + RNA
Expressing in E. coli
49 copies
4 nm
4 nm
CP monomer
CPR
TMV

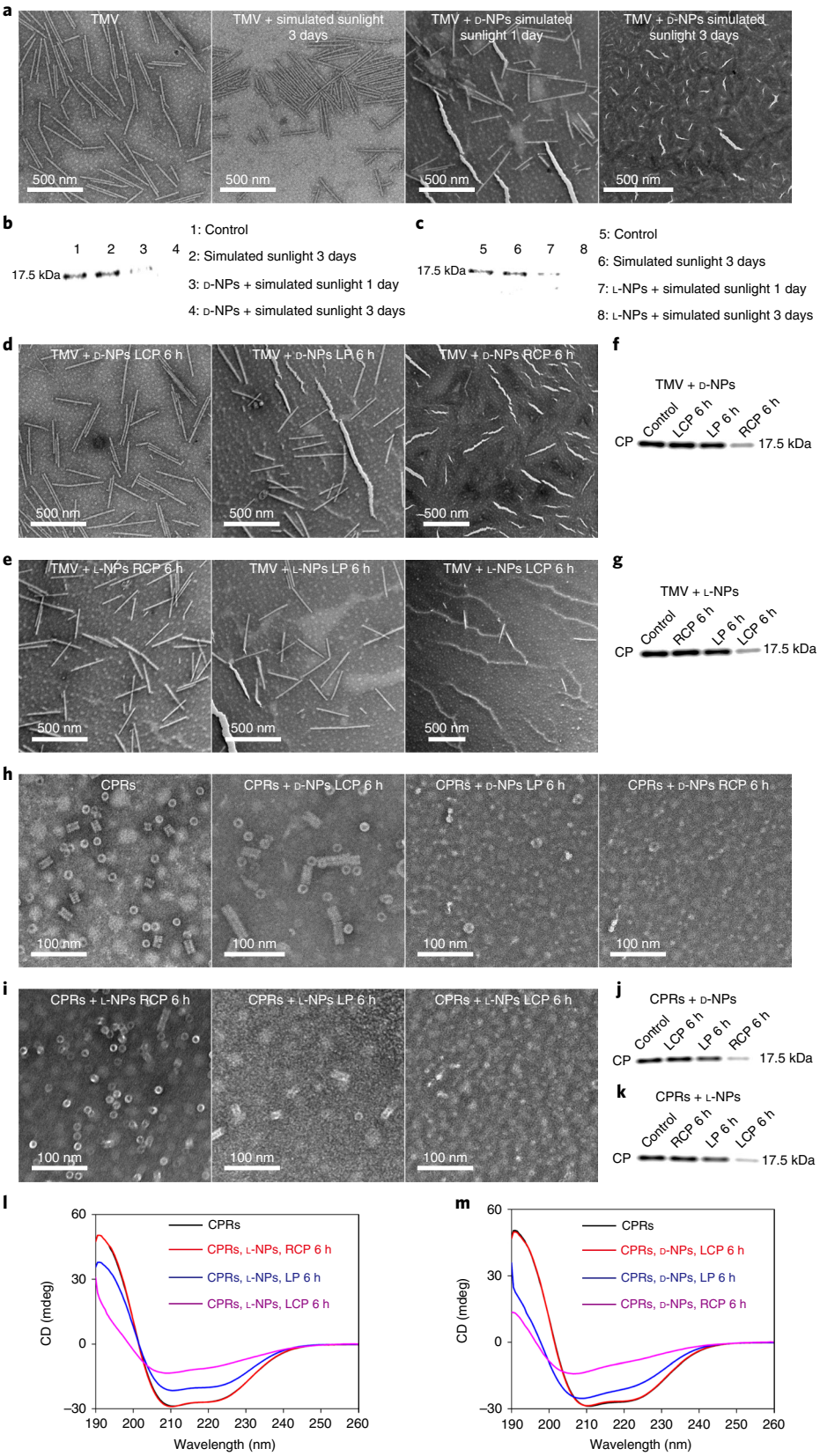

Fig. 2 | Circularly polarized light-response interaction between chiral nanoparticles and virus. a, TEM images of TMV treated under different conditions as specified in the images. **b**,**c**, Western blot analysis of TMV incubated with D-NPs (**b**) and L-NPs (**c**) under simulated sunlight for 3 days. **d**,**e**, TEM images of TMV incubated with D-NPs (**d**) or L-NPs (**e**) under LCP, LP and RCP for 6 h. **f**,**g**, Western blot analysis of TMV incubated with D-NPs (**f**) or L-NPs (**g**) under LCP, LP and RCP for 6 h. **h**,**i**, TEM images of CPRs incubated with D-NPs (**h**) or L-NPs (**i**) under LCP, LP and RCP for 6 h. **j**,**k**, Western blot analysis of CPRs incubated with D-NPs (**j**) or L-NPs (**k**) under LCP, LP and RCP for 6 h. **l**,**m**, CD spectra of CPRs incubated with D-NPs (**l**) or L-NPs (**m**) under LCP, LP and RCP for 6 h. All experiments were performed in triplicate.

Table 1 | The photolysis efficiency of TMV and CPRs by chiral NPs

Type of NPs	Substrate	Light at 532 nm	Efficiency ± s.d. (%)
D-NPs	TMV	RCP	93.8 ± 4.3
D-NPs	TMV	LP	33.7 ± 2.0
D-NPs	TMV	LCP	0.0 ± 0.0
L-NPs	TMV	LCP	87.8 ± 2.9
L-NPs	TMV	LP	26.8 ± 1.6
L-NPs	TMV	RCP	0.0 ± 0.0
rac-NPs	TMV	LP/LCP/RCP	0.0 ± 0.0
D-NPs	CPRs	RCP	98.4 ± 5.2
D-NPs	CPRs	LP	61.2 ± 2.9
D-NPs	CPRs	LCP	0.0 ± 0.0
L-NPs	CPRs	LCP	88.6 ± 3.8
L-NPs	CPRs	LP	56.7 ± 3.2
L-NPs	CPRs	RCP	0.0 ± 0.0
rac-NPs	CPRs	LP/LCP/RCP	0.0 ± 0.0
D-NPs	TMV	Simulated sunlight	93.6 ± 3.9
L-NPs	TMV	Simulated sunlight	82.8 ± 2.5

The efficiency was obtained from the image analysis quantifying the grey value of the band in triplicate SDS-PAGE or western blot experiments. The samples derive from the parallel experiments and those gels/blots were processed in parallel. Efficiency <1% was considered as no effect (0%).

Thus, we used D-NPs under RCP in most cases to investigate the mechanism of the photoreaction, since this combination of NP chirality and type of photons showed the highest efficiency of photocleavage of CPRs. When CPRs were incubated with D-NP dispersion containing 4 μM of the total amount of copper determined by inductively coupled plasma mass spectrometry (ICP-MS), and illuminated at 532 nm with a RCP beam for 6 h, a new distinct band was observed in SDS–polyacrylamide gel electrophoresis (SDS–PAGE) (Fig. 3a and Supplementary Figs. 7 and 9), suggesting that constitutive CP monomers were cleaved at a specific site; the intensity of this SDS–PAGE band also progressively increased with time of illumination. The LC–MS chromatogram showed peaks at three retention times of 13.5, 15.8 and 16.7 min (Fig. 3c–f) that were assigned to two CP fragments of 6 kDa and 11.5 kDa and an intact CP monomer of 17.5 kDa. L-NPs also cleaved CPRs under LCP resulting in the same products albeit with considerably lower efficiency (Fig. 3b and Supplementary Fig. 8). Obvious changes in the optical properties, geometry and elemental composition of the NPs were also observed (Supplementary Fig. 10).

Site-selective protein cleavage. To determine the cleavage site, the original protein and 11.5 kDa fragment were sequenced (Fig. 3g), which pointed to the bond between Asn 101 (N101) and Pro 102 (P102) as the cleavage site. To prove the recognition between the protein sequence around the N101–P102 site and chiral NPs, a total of 27 peptide sequences (Pep 1–27) were synthesized and tested for interaction with NPs (Table 2). Pep 1–4 had been cleaved specifically and at the same site between N101 and P102 (Fig. 3h–k and Supplementary Table 1), but the NPs were unable to break many other peptides, for example, Pep 5–9 (Supplementary Table 2), which cumulatively indicated that heptapeptide QANPTTA (that is, Gln 99, Ala 100, Asn 101, Pro 102, Thr 103, Thr 104 and Ala 105) was the sequence in CP that was recognized by the chiral NPs. Each amino acid of the QANPTTA sequence was then mutated to test this specificity (Supplementary Tables 3–5). We found that the starting amino acid, Gln (Q), could be replaced by any amino acid except Asn (N); and the third amino acid, Asn (N), could be replaced by Gln (Q); and the fifth and sixth amino acid, Thr (T), could be replaced by Ser (S). In a more general way, the results show that the XAN(Q)PT(S)T(S)A sequence can be selectively recognized by D-NPs.

As a negative benchmark experiment, NPs stabilized by cysteine (Cys), a dipeptide (cysteine–phenylalanine, CF) and glutathione (GSH) were unable to destroy CPRs. One of the reasons was that the NP diameters in these cases exceeded the 4 nm pore size of the CPRs (Supplementary Fig. 11). Similarly, when ligand (rac-Pen, Cys, CF, GSH)-stabilized NPs were mixed with CPRs under CPL, we observed no changes in CD spectra or in the shape of the NPs (Supplementary Figs. 12–14). We also found that surface ligands alone, for instance, L-Pen or D-Pen, were not able to cleave the virus under any conditions (Supplementary Fig. 15).

It is also informative to compare the virucidal activity of copper sulfide NPs with those made of gold[42]. GSH-functionalized gold nanoclusters (Au NCs) with an average diameter of 2.5 ± 0.41 nm were made according to the previously established protocol[43] and tested under the same conditions. They can serve as a convenient benchmark for small NPs that can geometrically fit into the rod-like 4 nm cavity but do not attach to the protein rings of the virus strongly enough and specifically enough for the site-selective cleavage to take place. The TEM images (Supplementary Fig. 16) indicate that Au NCs do not enter the capsid cavity effectively, most probably due to lack of strong chemical affinity to the peptide sequence and improper conformation of GSH to make sufficiently dense network of hydrogen bonds.

To further examine the specificity of peptide cleavage by chiral NPs, several other proteins that do not have sequences resembling XAN(Q)PT(S)T(S)A, such as BSA, were tested. We found that BSA could not be photocleaved by any of our chiral NPs under 532 nm CPL (200 mW) of any helicity (Supplementary Fig. 17) under conditions similar to CPR experiments, thereby confirming their site- and protein-selectivity. We also tested the coat proteins of brome mosaic virus (BMV CP) and simian virus 40 (SV40 CP) and found no site-selective or other type of photoinduced cleavage of these typical plant viruses.

To confirm the universality of the specific cleavage of peptides, three other proteins, namely GSPK–GSPI–GSPJ complex from the toxigenic *E. coli* Type 2 Secretory System (34 kDa), cell adhesion protein from oocytes (56 kDa) and human rotavirus coat protein (35 kDa), which have LAQPTTA, QAQPTSA and TANPTTA sequences, respectively, were also tested using our NPs. All these proteins were split into two fragments after mixing with D-NPs and RCP light illumination (Supplementary Fig. 18).

Origin of site-specificity. To understand how the chiral NPs interact with components of the TMV capsid with and without light, we first investigated the thermodynamics of their binding to CPRs using isothermal titration calorimetry (Fig. 4a,b and Supplementary Fig. 19). The affinity constants, K_a, for the binding of D-NPs to CPRs and QANPTTA were $(2.78 \pm 0.32) \times 10^7$ and $(3.26 \pm 0.20) \times 10^7$, respectively. The K_a for L-NPs with CPRs and QANPTTA were $(1.57 \pm 0.26) \times 10^6$ and $(1.55 \pm 0.14) \times 10^6$, respectively, which are ~20 times smaller than those for D-NPs. Even weaker binding with CPRs was observed for rac-NPs with $K_a = (9.07 \pm 0.64) \times 10^3$, for Cys-stabilized NPs with $K_a = (5.43 \pm 0.29) \times 10^3$, for CF-stabilized NPs with $K_a = (7.02 \pm 0.34) \times 10^3$ and for GSH-stabilized NPs with $K_a = (4.17 \pm 0.20) \times 10^3$ (Supplementary Fig. 20). Considering the selectivity of virucidal action, other proteins, such as BSA, BMV CP and SV40 CP, also showed very limited affinity for our NPs, with K_a values ranging from 2.07×10^3 to 8.12×10^3 (Supplementary Fig. 21). A cumulative analysis of these data and those in Supplementary Table 6 led us to firmly conclude that, in addition to

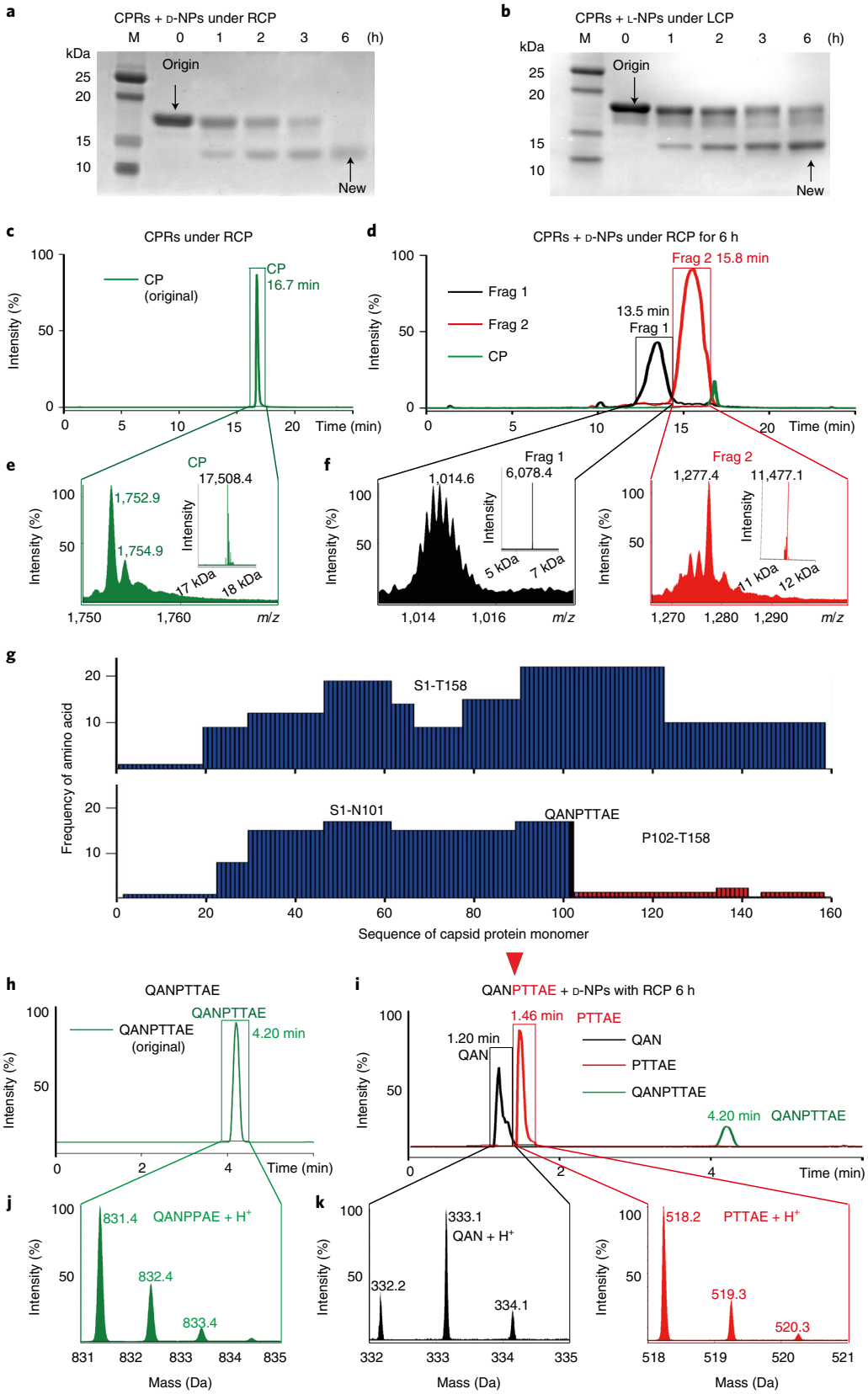

Fig. 3 | Cleavage site analysis. a,**b**, SDS–PAGE for D-NPs incubated with CPRs under 532 nm RCP (**a**), and for L-NPs incubated with CPRs under 532 nm LCP for different times (**b**). **c**, LC–MS of CPR incubated without NPs under RCP for 6 h. **d**, LC–MS of CPRs incubated with D-NPs under RCP for 6 h. **e**, High-resolution representation of the peak at 16.7 min due to elution of CP. **f**, High-resolution representation of the peaks at 13.5 and 15.8 min due to the photocleavage products Frag 1 and Frag 2. **g**, Sequence analysis of bands from the original CP and the large fragment (Frag 2). **h**, LC–MS of the QANPTTAE octapeptide. **i**, LC–MS of QANPTTAE incubated with D-NPs under 532 nm RCP for 6 h. **j**, MS of QANPTTAE. **k**, MS of QAN and PTTAE. All experiments were performed in triplicate.

Table 2 | Sequence-specific cleavage for different peptide mutations (n = 3)

Name	Amino acid sequence	Photocleave (yes or no)	Site	Mutation
Pep 1	EVENQANPTTAET	Yes	N P	No
Pep 2	NQANPTTAETLD	Yes	N P	Shorten
Pep 3	QANPTTAE	Yes	N P	Shorten
Pep 4	QANPTTA	Yes	N P	Shorten
Pep 5	ANPTTAE	No		Shorten
Pep 6	NPTTAE	No		Shorten
Pep 7	PTTAE	No		Shorten
Pep 8	QANPTT	No		Shorten
Pep 9	QANP	No		Shorten
Pep 10	AANPTTA	Yes	N P	Q1 to A1
Pep 11	QGNPTTA	No		A2 to G2
Pep 12	QAAPTTA	No		N3 to A3
Pep 13	QANATTA	No		P4 to A4
Pep 14	QANPATA	No		T5 to A5
Pep 15	QANPTAA	No		T6 to A6
Pep 16	QANPTTG	No		A7 to G7
Pep 17	EANPTTA	Yes	N P	A1 to E1
Pep 18	VANPTTA	Yes	N P	A1 to V1
Pep 19	HANPTTA	Yes	N P	A1 to H1
Pep 20	TANPTTA	Yes	N P	A1 to T1
Pep 21	NANPTTA	No		A1 to N1
Pep 22	QAQPTTA	Yes	Q P	N3 to Q3
Pep 23	NAQPTTA	No		Q1 to N1
Pep 24	QANPSTA	Yes	N P	T5 to S5
Pep 25	QANPTSA	Yes	N P	T6 to S6
Pep 26	QANPSSA	Yes	N P	T5 to S6 T6 to S6
Pep 27	NAQPSSA	No		Q1 to N1, T5 to S5, N3 to Q3, T6 to S6

the host–guest geometric match, the high specific binding between CPRs and chiral NPs leads to the site-specific CP cleavage.

Molecular dynamics (MD) simulation and quantum mechanical (QM) calculations further uncovered essential atomistic details of the photocleavage process. Confirming earlier expectations, a 250 ns MD simulation showed that NPs can easily enter the water-filled pore of the TMV capsid, forming a complex with the CP monomer via supramolecular bonding with a large electrostatic component due to the carboxylate of the Glu 106 side chain and the secondary amine of D-Pen. Additionally, hydrogen bonds between the amide oxygens of Gln 99, Ala 100, Pro 102 and Glu 106, and the amine hydrogen of D-Pen also formed (Fig. 4c,e and Supplementary Figs. 22–25). In the case of L-NPs, only hydrogen bonds with Asn 101, Thr 103 and Glu 106 (Fig. 4d and Supplementary Fig. 26) can be formed because of the stereochemical frustration, which inevitably leads to weaker binding and smaller K_a. Peaks in the radial distribution functions display higher intensities for D-NPs than for L-NPs (Supplementary Fig. 27), confirming the tighter binding of the former and explaining the difference in photocleavage rates between the NPs of the two chiralities.

Photoinduced cleavage due to electron transfer. The geometry of the NP–CPR complex identified from MD data (Fig. 4c,d), combined with QM methods, allowed us to gain insight into the electronic processes leading to the selective photocleavage after binding to the CP. We analysed the charge distribution under 530-540 nm light in peptide–NP complexes based on the equilibrium atomic configuration from MD simulations. Polarization maps arising from the electronic excitation of D-NPs and L-NPs displayed strikingly different patterns (Fig. 4f,g). In the case of the L-NP–QANPTTAE complex, the negative potential isosurface is located far away from the cleavage sites, while the same isosurface for the D-NP–QANPTTAE is larger and overlaps with the cleaving sites. We used the Cartesian coordinates of the points to compare their nanoscale chirality. Osipov–Pickup–Dunmur chirality measures calculated for the isosurfaces of D-NPs and L-NPs were +3.080 and −0.064, respectively. Thus, the light-induced polarization fields dramatically differ in atomic localization, chirality (that is, value) and handedness (that is, sign). The CD spectra for the microstates responsible for peptide lysis are also different (Supplementary Fig. 28). These spectra are not exact mirror images because both systems, and therefore the efficiency of photocleavage, depend on the polarization of incident photons, which is observed experimentally (Fig. 2 and Table 1). The dependence of the photocleavage efficiency on the polarization of the incident light is a direct consequence of the difference in chirality of the electronic states of the two complexes being excited by 532 nm light.

We found that reactive oxygen species (ROS), identified as singlet oxygen radicals from the data of ROS inhibition by NaN_3 and ESR spectra, were generated under illumination independently of

QANPTTA or CPRs (Supplementary Fig. 29). It is important to point out that singlet oxygen radicals are the side product of the photocatalytic reaction and are generated via energy transfer[44–46] (Fig. 4h), and are not involved in peptide hydrolysis. This conclusion is supported by several experimental and theoretical findings. First, the transfer of photonic energy from excitons in NPs to other chemical structures occurs over long distances (~2 nm)[44] which is described by polarization isosurfaces in Fig. 4f,g. Both oxygen molecules and amino acids can be resonantly excited by the excitons in NPs; when a triplet oxygen molecule serves as an acceptor, an excited singlet oxygen is produced. For chiral NPs in TMV cavities, the majority of ROS is singlet oxygen and thus generated by energy transfer. Second, unlike hydroxyl radicals, which are well known for their ability to cleave proteins, the reactivity of singlet oxygen radicals is lower that of hydroxyl radicals, which are therefore unable to cleave proteins[47]. Third, a selective cleavage reaction takes place when hydroxyl radicals are localized on the surface of the catalyst[47]. However, the polarization profiles in Fig. 4f,g showed that the area of formation of ROS was delocalized. Besides encompassing a large volume that makes selective cleavage of the bond by them impossible, these data indicate that ROS are generated far away from the QANPTTA cleavage site. No evidence that singlet oxygen radicals are bound to specific sites on NPs or the peptides was obtained. Finally, the LC–MS data also confirmed that ROS are not directly involved in the cleavage of protein or peptides; in fact, the sum of the molecular weights of two cleaved fragments minus the molecular weight of H_2O coincides with the molecular weight of the original peptide. This indicates that lysis of the peptide bond occurs via peptide hydrolysis rather than oxidative cleavage induced by ROS (Fig. 3h–k and Supplementary Tables 1–5).

Combined with the results that cleavage was accompanied by the oxidation of Cu^+ and subsequent N–Cu^{2+} coordination (Supplementary Figs. 10 and 30), we concluded with certainty that the photocleavage was initiated by electron transfer, which leads to a hole, and conversion of Cu^+ to Cu^{2+}. Electron transfer leading to the short-lived $O_2^{\cdot-}$ anion radical[45] was much less effective and occurs only over short distances (~0.2 nm) when triplet oxygen happens to be in close proximity to NPs. The probability of electron transfer is much lower than with energy transfer but results in the permanent Cu^{2+} catalytic site, which serves as the primary redox site initiating the proteolytic cleavage via formation of the coordination bonds with the cleavage site. The lifetime of the hole is short (~100 ps (ref. [48])) while the relaxation of the secondary structure of the protein is long, often exceeding 100 ns (ref. [49]), making it unlikely that accumulation of holes under illumination in free NPs not associated with CPR into a supramolecular complex contributes to the photocleavage. The binding energy of other elements (oxygen, sulfur) did not change obviously (Supplementary Fig. 30). Additional evidence for the electron transfer were the data on transient absorption spectroscopy (Supplementary Fig. 29). The absorption recovery time at 530 nm of radiation was 602 fs for free D-NPs, and 398 and 486 fs for D-NPs with CPRs and QANPTTA, respectively, supporting photocleavage via electron transfer (Supplementary Fig. 29). The transient holes also were detected using ESR after photoexcitation of NPs, while significantly decreased holes in the presence of CPRs further confirmed photocleavage via electron transfer (Supplementary Fig. 29). This also partly explains why the Cu^+ to Cu^{2+} transition only seems to happen in the presence of the correct substrate (Supplementary Fig. 30). In addition, peptides adhering to the surface of the NPs alter the balance between energy and electron transfer pathways primarily by changing the dielectric constant of the media[50]. When the peptides bind strongly to the NPs, the environment within the critical distance of 0.2 nm from the NP surface changes dramatically. Water has a high dielectric constant of $\varepsilon = 78$, whereas peptides have low dielectric constants of $\varepsilon = 6–7$ (ref. [51]). A drastic increase in the electrostatic interactions facilitates electron transfer to all species within the low-dielectric-constant medium[50,52]. NP and peptides were separated when the incorrect substrate was present. This suppressed electron transfer and hole oxidation.

Overall, singlet oxygen radicals and the QANPTTA cleavage are spatially segregated. Singlet oxygen radicals were the product of the electron transfer and were irrelevant to peptide cleavage. Photocleavage was initiated by electron transfer, which generated permanent Cu^{2+} active sites, although few ROS were generated compared to energy transfer.

Site-selective lysis of CP occurs because of the chirality-dependent binding of NPs to the peptide segments driven by both hydrophobic interactions and electronic polarization. Within the capsid cavities of TMVs, NPs may dynamically interact with many CP monomers via labile hydrogen bonds, but the NP complex with a specific QANPTTA sequence on a specific CP monomer becomes locked-in when the short-range hydrophobic interactions are engaged. Then the distance between the copper ions on the surface of NP and the peptide bond at the proteolytic site shortens and becomes susceptible to hydrolysis (Fig. 4h–k). Our DFT calculations showed that the methylene residues in Pro 102 at the D-NP interface point outwards to form a tight hydrophobic pocket with Pen ligands (Supplementary Fig. 31), which leads to high K_a values (Fig. 4a,b and Supplementary Fig. 18). L-NPs also interact with the hydrophobic Pro 102 ring, but in a more hydrophilic surface region. When the distance from the surface of Asp 101–Pro 102 to the redox-active Cu^{2+} atoms is longer, the activation of the peptide bond surrounding water molecules for hydrolysis by L-NPs is less effective, and consequently the proteolytic cleavage is less effective.

Fig. 4 | Mechanism of the selective photocleavage of CP by chiral NPs. a,**b**, Isothermal calorimetry data for CPRs and QANPTTA forming host–guest complexes with D-NPs (**a**) and L-NPs (**b**). All the experiments were performed in triplicate. **c**,**d**, MD simulation of the host–guest complex for CPRs with D-NPs (**c**) and L-NPs (**d**). **e**, Atomistic details of interaction between D-NPs and CP. **f**,**g**, Isosurfaces for average electrostatic polarizations of D-NPs (**f**) and L-NPs (**g**) interacting with multiple QANPTTA segments of CP monomer in TMV capsid being illuminated with the light in the spectral window from 530 to 540 nm. Red surface represents the regions with an isovalue of −4 mV and depict the QM localization of negative charge after light absorption; blue surfaces are the regions with an isovalue of +4 mV and depict the quantum mechanical localization of positive charge after light absorption. The locations of the Asn 101–Pro 102 sites are highlighted by thickened chemical bonds of light blue. **h**, Excitation, energy and charge-transfer processes between chiral CuS NPs and surrounding chemical structures. Generation of ROS occurs via two mechanisms: energy transfer that leads to singlet oxygen and electron transfer that leads to oxygen anion radical. Energy transfer also takes place between the peptides and the NPs. The characteristic distances for energy and electron transfer are very different: ~2 nm for the former and ~0.2 nm for the latter. **i**,**j**, Polarization maps for the Ala 100–Asn 101–Pro 102–Thr 103 fragment (ANPT), which is the closest to the surface of the chiral NPs, interacting with D-NP (**i**) or L-NP (**j**). Atoms are coloured according to the change in the electronic population upon excitation at 533–534 nm (red, −0.002e; blue, +0.002e). The cleavage site is depicted as a thicker translucent surface. **k**, Molecular organization of the D-NP–peptide complex for the ANPT fragment. **l**, Molecular organization of the L-NP–peptide complex for the ANPT fragment. Hydrophobic and hydrophilic regions in **k** and **l** are marked in white and blue, respectively. **m**, Bond length for the Asn 101–Pro 102 peptide bond during the DFT geometry optimization for D-NP (red) and L-NP (black) interacting with the closest ANPT fragment (ANPT). The insets depict the optimized geometry of the Asn 101–Pro 102 fragments, the dihedral angle between the peptide bond and Pro 102 ring, and the bond order of the peptide bond in each case.

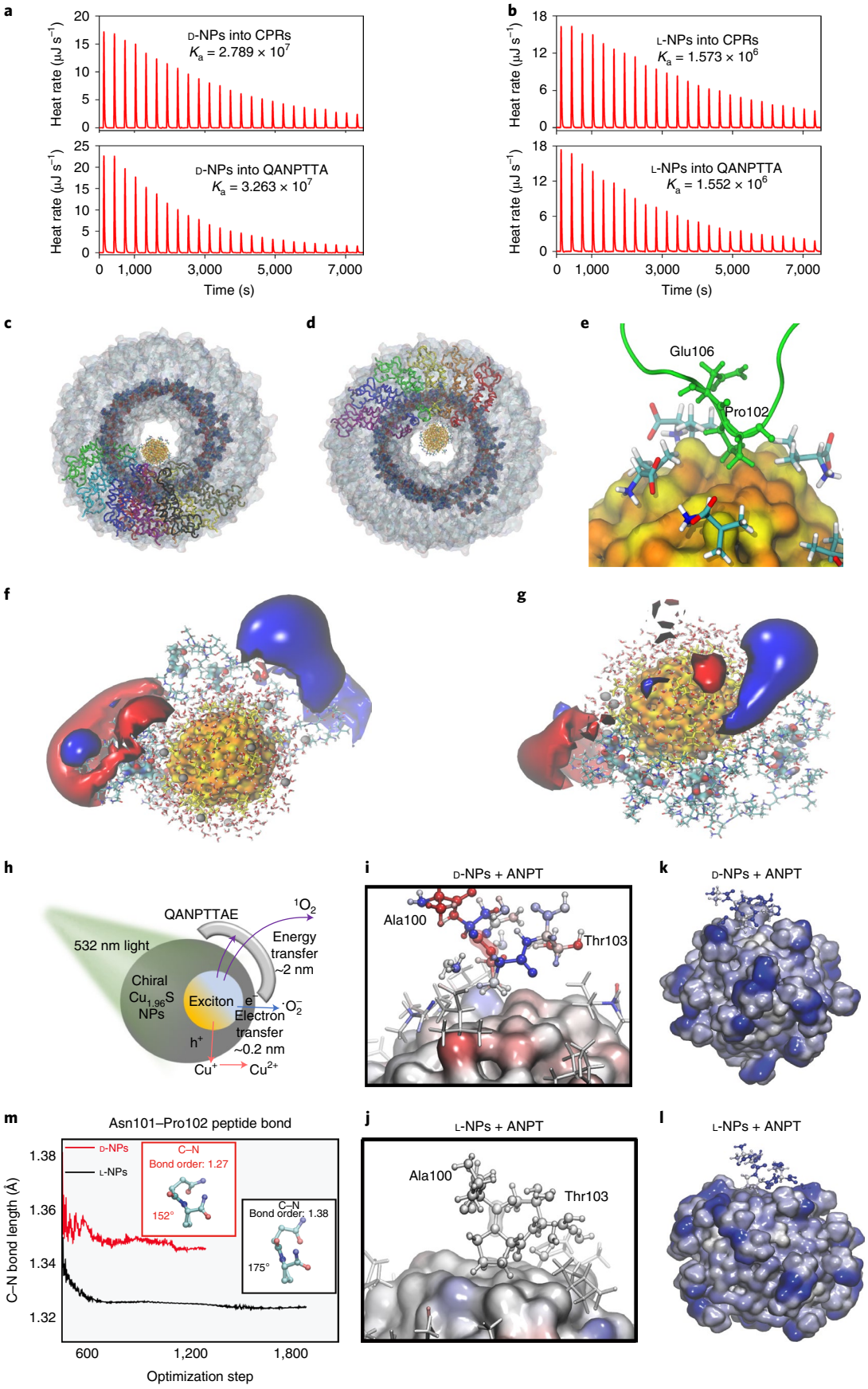
a
Heat rate (μJ s−1)
D-NPs into CPRs
Ka = 2.789 × 10^7
D-NPs into QANPTTA
Ka = 3.263 × 10^7
Time (s)
b
L-NPs into CPRs
Ka = 1.573 × 10^6
L-NPs into QANPTTA
Ka = 1.552 × 10^6
c
d
e
Glu106
Pro102
f
g
h
QANPTTAE
532 nm light
Chiral Cu1.96S NPs
Exciton
Energy transfer ~2 nm
Electron transfer ~0.2 nm
i
D-NPs + ANPT
Ala100
Thr103
k
D-NPs + ANPT
m
Asn101–Pro102 peptide bond
D-NPs
L-NPs
C–N Bond order: 1.27
152°
C–N Bond order: 1.38
175°
C–N bond length (Å)
Optimization step
j
L-NPs + ANPT
Ala100
Thr103
l
L-NPs + ANPT

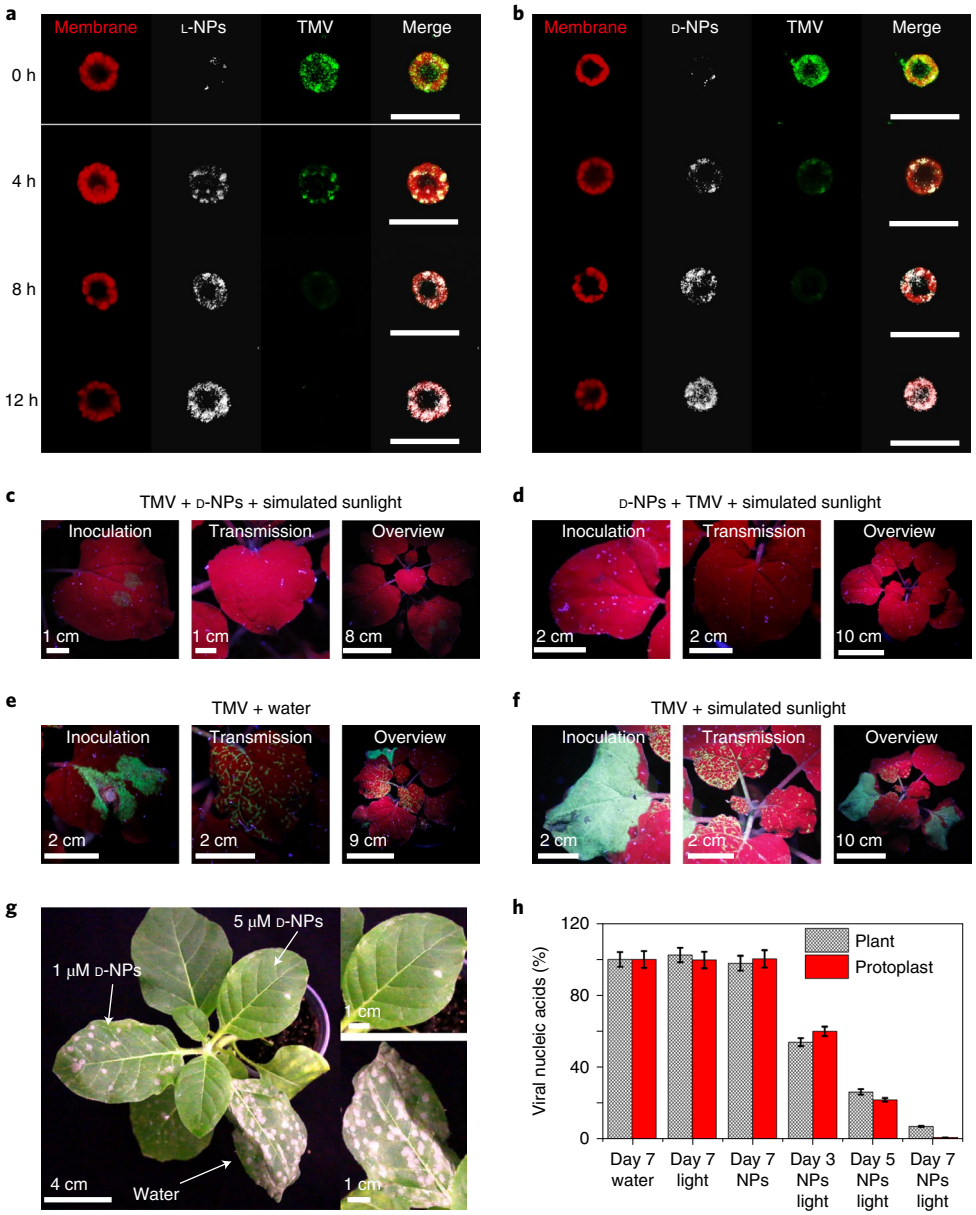

Fig. 5 | Photocleavage of virus by D-NPs in protoplasts and plants. a, Representative confocal microscopy images of L-NPs incubated with protoplast from *N. tabacum* NC89 plants infected with TMV and then illuminated with simulated sunlight (2,000 lux illuminance) for different time periods. **b**, Representative confocal microscopy images of D-NPs incubated with protoplast from *N. tabacum* NC89 plants infected with TMV and then illuminated with simulated sunlight (2,000 lux illuminance; membrane refers to the protoplast's cell membrane) for different time periods. Scale bars, 50 μm. **c**–**f**, In vivo imaging of *N. benthamiana* plants after treatment with GFP-TMV via *Agrobacterium* inoculation. **c**, *N. benthamiana* was first inoculated with GFP-TMV and, 24 h later, the plants were treated with D-NP dispersion with a total copper content of 5 μM and illuminated with simulated sunlight for 7 days. **d**, *N. benthamiana* was first sprayed with D-NP dispersion with a total copper content of 5 μM and, 24 h later, the plants were inoculated with GFP-TMV and illuminated with simulated sunlight for 7 days. **e**, *N. benthamiana* was inoculated with GFP-TMV and 24 h later sprayed with water and treated with simulated sunlight for 7 days without chiral NPs. **f**, *N. benthamiana* was inoculated with GFP-TMV and 24 h later treated with simulated sunlight for 7 days without chiral NPs. **g**, Photographs of infected *N. tabacum* cv. Samsun^{NN} sprayed with different concentrations of chiral NP dispersions with a total content of copper content of 1 μM and 5 μM after 3 days under simulated sunlight. **h**, Content of viral nucleic acids extract from protoplasts and plants after different treatments. Data are presented as mean ± s.d. ($n = 3$) with the error bars representing the s.d. Certain outlier plants were excluded from the experiments.

Looking at the atomistic details of peptide bond activation, NP–peptide complex formation was accompanied by conformational changes in the Pro 102 ring, which remained nearly coplanar with respect to the peptide bond with the Asn 101 residues. This led to L-NPs with higher bond order and shorter bond lengths compared with those of D-NPs (Fig. 4l). These differences strongly affect the ability of 1*s* orbitals of the methylene hydrogen atoms to contribute electrons to the π orbitals that confer double-bond character on the peptide bond, with a larger superposition if the ring is properly aligned with the bond. Therefore, even in the ground state, the D-NPs weaken the peptide bond between Asn 101 and Pro 102. Illumination leads to additional activation of this bond and occurs to a greater extent for D-NPs than for L-NPs (Fig. 4l). The electronic population on the nitrogen atom in Pro 102 increases dramatically

in the complex with D-NP, rendering this atom susceptible to interaction with water molecules[53]. The mechanism of lysis was further confirmed by the lack of supramolecular interactions between chiral NPs and mutated peptide (QANGTTAE), in which the Pro 102 is replaced with glycine 102 (Gly 102) (Supplementary Fig. 30). As mentioned above, the strong binding between suitable peptides and NPs decreased the dielectric constant of the media around the NPs and facilitated the electron transfer pathways. NP and peptides were separated when the incorrect substrate was present. This suppressed electron transfer and hole oxidation. Finally, we tested for the ratio between the number of moles of cleaved peptides and moles of copper atoms in the NPs. Based on the final hydrolysis yield, the concentration of hydrolysed peptide is 14.3 μM, whereas the total content of copper ions (both Cu^{+} and Cu^{2+}) is 4 μM, confirming that the reaction is catalytic rather than stoichiometric.

Testing of TMV photocleavage in vitro and in vivo. NP dispersions containing a total copper concentration of less than 500 μM as determined by ICP-MS did not reduce the viability of cultured protoplasts or plants of *Nicotiana tabacum* (Supplementary Figs. 32 and 33). We also found that spraying was an efficient method of treating plants with NPs, clearly indicating that NPs enter the stoma and then the plant cells, which is consistent with previously reported data[54,55] (Supplementary Fig. 34).

Protoplasts from *N. tabacum* infected with TMV (Fig. 5a) were incubated with D- or L-NP dispersions with a total copper content of 5–20 μM under simulated sunlight with illuminance of 2,000 lux and a spectral range from 400 to 750 nm. Confocal microscopy images showed that the green fluorescence, representing TMV, was gradually diminished with illumination. D-NPs showed markedly better antiviral activity than L-NPs both in protoplast and full plants (Fig. 5 and Supplementary Fig. 35). The green-fluorescent-protein-labelled TMV (GFP-TMV) was used to infect 4-week-old *Nicotiana benthamiana* plants via agrobacterium inoculation. The plants were subsequently sprayed with D-NPs and then illuminated with simulated sunlight for 7 days (2,000 lux illuminance, 16 h/8 h photoperiod, which corresponds to the light period (16 h) and the dark period (8 h) of the circadian cycle). Non-infected plants were initially sprayed with D-NP dispersions with a 5 μM total content of copper and, 24 h later, GFP-TMV was inoculated. The plants were then illuminated with simulated sunlight every day for 7 days (2,000 lux illuminance, 16 h/8 h photoperiod).

After treatment with D-NPs (Fig. 5b, c), the inoculated leaves displayed much weaker fluorescence from GFP-TMV than the ones without NP treatment; there was no transmission through stems and veins. As the concentration of chiral NPs increased, the curing effect was also enhanced (Fig. 5f) in line with the proposed mechanism of the virucidal activity. The control plant sprayed only with water showed severe leaf curling in new leaves, indicating rapidly spreading GFP-TMV infection (Fig. 5d,e). RNA and protein extracted from the leaves of *N. benthamiana* were also analysed by reverse transcription polymerase chain reaction (RT–PCR) and western blotting (Fig. 5g and Supplementary Fig. 35). The viral nucleic acids decreased by 98.7% in protoplasts and 92.6% in plant on day 7 after treatment. These findings demonstrated that D-NPs inhibited TMV and prevented viral infection in living plants, and they are more efficient than currently used or emergent anti-TMV agents[56–59] (Supplementary Fig. 36). A hypersensitive response was also avoided, while the control leaves that did not receive D-NP treatment exhibited a high hypersensitive response (Fig. 5f). Finally, the post-treatment biodistribution of copper from fruits to roots was analysed by ICP-MS. There were no significant increases of copper content in the roots, stems or fruits in agreement with biodistribution data on other nanomaterials[58–60], such as carbon nanotubes[61]. There was also no significant difference in copper content in the leaves compared with the control plants without NP exposure. Due to the small amounts of NPs required to suppress TMV, the preliminary tests for the total content of copper in the soil samples did not reveal a significant change (Supplementary Figs. 37–40): it was consistent with the original total copper content of 7 mg kg^{-1} and remained far below agricultural safety standards for the total copper content, set at 20 mg kg^{-1} (ref. [62]).

Conclusions

We demonstrated that Pen-ligand-functionalized chiral $Cu_{1.96}S$ NPs could serve as effective photoactivated antivirals for plants and established a detailed mechanism of their virucidal action. Thermodynamic measurements and multimodal computations show that the surface chirality and collective non-covalent interactions of the minimally decorated NPs represent a potent toolbox for imparting selectivity to target proteins because of their site-specific supramolecular bonding with peptide chains. The photocleavage in an incident-photon-dependent way originates from chiral NPs with circularly polarized photons from excited states. This finding reveals important aspects of light–matter interaction between chiral NPs and biomolecules, which can be utilized for further fundamental and mechanistic studies. Notwithstanding open questions relating to the suitability and environmental-friendliness of chiral NPs for food production, the data obtained for $Cu_{1.96}S$ NPs carrying Pen provide fundamental foundations for the engineering of nanomaterials for mitigation of agricultural viral threats. Given the simplicity of the NP synthesis, the possibility of reducing the cumulative environmental effects associated with traditional pesticide production offer an additional incentive for the further development of this technology.

Methods

Synthesis of D-NPs, L-NPs and rac-NPs. The synthesis of D-NPs, L-NPs and rac-NPs was based on a previously published method with modifications[63]. The Pen ligands were recrystallized. Specifically, L- and D-Pen were fully dissolved in a minimal amount of 1 M HCl and then quickly transferred into a 4 °C bath to crystalize. This procedure was repeated three times.

Next, 35 ml of ultrapure water was heated to 95 °C in a three-neck flask (100 ml) and protected by nitrogen under magnetic stirring for 30 min to eliminate residual oxygen. $CuCl_2{\cdot}2H_2O$ (0.2 mol l^{-1}, 2 ml) was injected using a syringe while stirring and continuously purging the reaction medium with nitrogen for 5 min. Recrystallized D- or L-Pen (0.4 mmol, 0.06 g) powder was quickly added to the flask with stirring under nitrogen for 30 min. After the temperature was cooled to 30 °C, $NaBH_4$ (0.1 mol l^{-1}, 5 ml) and D- or L-Pen (0.01 mol l^{-1}, 4 ml, source of sulfur) were quickly injected by syringe.

After reacting for 12 h in a nitrogen atmosphere, a dark red solution was formed, indicating the formation of D- or L-Pen-modified NPs. The solution was purified by centrifugation (6000 *g*, 10 min) at room temperature with isopropanol and resuspended in H_2O or PBS (0.01 M, pH 7.4) for further use. For the synthesis of rac-NPs, equimolar amounts D- and L-Pen (each 0.2 M, 200 μl) were used in the synthesis.

The copper content in chiral NPs. The total copper content in NP dispersions was used to express the concentration for agricultural and related experiments according to the conventions used in this field of science. Specifically, 4 ml of nitric acid (65–68%, Aladdin) was added to 1 ml of purified NPs (resuspended in ultrapure water) and heated at 120 °C for 4 h. After cooling down to room temperature, the solution was made up to 20 ml with ultrapure water. Then, 9 ml of ultrapure water was added to 1 ml of the above solution for ICP-MS detection. In the experiments, ultrapure water was used as the background. Data were obtained with an ICAP TQ (Thermo Fisher, Germany).

Expression of recombinant CPRs. CPRs were obtained by a previous protocol[64]. A wild-type CPR gene optimized for the codon usage of *E. coli* was purchased from Sangon Biotech and amplified with PCR using two pairs of primers (P1, 5′-AGATATACATATGAGCTATAGCAT-3′ and P2, 5′-GTTTCCGCGGTACACGGATTGGCCT-3′; P3, 5′-AGGCCAATCCGTGTACCGCGGAAAC-3′ and P4, 5′-GGAATTCTCAGGTCG CCGGGCC-3′). The CPR was made by overlap. The CPR gene was then cloned into the pET32a (+) vector (Novagen) at the NdeI–EcoRI restriction sites, verified by sequencing (Shanghai Invitrogen Biotechnology), and then transformed into *E. coli* BL21 (DE3) strain (Novagen) for expression and purification of recombinant CPRs.

CPRs or TMV cleavage by chiral NPs under simulated sunlight or CPL. CPRs or TMVs were suspended in PBS (0.01 M, pH 7.4) to a final concentration

of 1.5 mg ml^{-1}. CPRs or TMVs (30 µl of 1.5 mg ml^{-1}) were mixed with 30 µl of freshly synthesized NP dispersion in water with a total copper content of 4 µM. The mixture was incubated at 30 °C with shaking for 1 h in an artificial climate chamber (30 °C temperature, 60% relative humidity, 0 lux illuminance), and then transferred to a quartz cuvette with an optical path length of 1 cm in a bright environment (2,000 lux illuminance or a 532 nm laser with power of 200 mW). Sunlight was used as the light source to illuminate the mixture for 3 days (2,000 lux illuminance). The 532 nm laser was used as the light source and laser emission was converted into CPL by a linear polarizer and a quarter-wave plate with a transmission angle of $a \pm 45°$ to illuminate the mixture for different time periods (1, 2, 3 and 6 h, respectively).

The interactions between CPRs or TMV and rac-NPs or other ligand-stabilized chiral NPs under polarized light. CPRs or TMVs were suspended in PBS (0.01 M, pH 7.4) to a final concentration of 1.5 mg ml^{-1}. CPRs or TMVs (30 µl of 1.5 mg ml^{-1}) were mixed with 30 µl of rac-NPs in H_2O. The mixtures were incubated at 30 °C with shaking for 1 h, and then transferred to a quartz cuvette with an optical path length of 1 cm under illumination. For rac-NPs, a 532 nm laser (200 mW) was used as the light source; for Cys-NPs and CF-NPs, a 594 nm laser (200 mW) was used as the light source; for GSH-NPs, a 594 nm laser (200 mW) was used as the light source. All the laser emission were converted into CPL by a linear polarizer and a quarter-wave plate with a transmission angle of $a \pm 45°$ to illuminate the mixture for 6 h.

SDS–PAGE. SDS–PAGE was performed as follows: after CPL-assisted cleavage was complete, the chiral NPs and CPRs were separated by ultrafiltration centrifugation (100 kDa molecular weight cut-off, Millipore). The purified protein samples (30 µl) were mixed with 10 µl loading buffer and reacted for 1 h at 75 °C. After cooling to room temperature, samples (10 µl) were injected into each lane. Electrophoresis was performed at 120 V for 65 min. Electrophoretic images were captured with a Gel Doc XR+ Gel Documentation System (Bio-Rad).

CD and ultraviolet measurements. After reacting, the samples were directly characterized in a quartz cuvette. The temperature was maintained at 25 °C for all measurements, with a scanning range of 300 to 1,000 nm (for chiral NPs with a scan speed of 0.2 nm s^{-1}) and 190 to 260 nm (for organic matter with a scan speed of 0.005 nm s^{-1}) under high-purity nitrogen. At the same time, the CD spectra of air and solvents were also obtained and used as the baseline. The CD and ultraviolet–visible spectra were obtained, together with Chirascan-Plus quantitative CD spectra, and processed with OriginLab software (Applied Photophysics).

Fluorescence measurements. Due to the presence of Tyr and Trp, the protein can emit fluorescence at about 330 nm when excited at 280 nm. The luminescence intensity of protein was recorded using an F-7000 fluorescence spectrophotometer (Hitachi) and a scan range from 290 to 400 nm.

TEM imaging. The CPRs (15 µl of 0.5 mg ml^{-1}) were adsorbed onto glow discharge grids (300 mesh carbon-coated copper grids) for 5 min and rinsed with three drops of PBS (10 mM, pH 7.4). The rinsed grids were floated with phosphotungstic acid solution (10 µl, 10 mM, pH 6.0) for another 5 min, fixed with glutaraldehyde (0.25%) and then blotted dry with filter paper. The images were captured by a TEM (JEOL JEM-2100) operating at an acceleration voltage of 120 kV.

Detection of ROS. The amount of ROS generated by the chiral NPs with CPRs under 532 nm CPL was assessed with a 2′,7′-dichlorodihydrofluorescein probe. 2′,7′-Dichlorodihydrofluorescein at a final concentration of 20 µM in DMSO was mixed with 30 µl of 4 µM copper and 30 µl of 1.5 mg ml^{-1} CPRs in PBS, and irradiated at RCP/LCP for various time periods. After irradiation, the mixture was separated by ultrafiltration centrifugation (100 kDa for 10 min). The fluorescence spectrum of the supernatant solution was recorded under excitation at 485 nm.

ESR measurements. The ESR spectrum is considered to represent the most direct evidence when identifying the ROS generated. To further confirm the generation of ROS by chiral NPs, we used 2,2,6,6-tetramethylpiperidine as the trapping agent. In addition, the chiral NPs were examined for production of different ROS using the ESR technique at different visible light irradiation time periods (0, 3, 5 and 10 min). Singlet oxygen and holes data were acquired with an EMXplus-10/12 ESR spectrometer (Bruker, Germany).

ITC measurements. Chiral NPs were purified by centrifugation with isopropanol and resuspended in PBS (10 mM, pH 7.4) to give an NP concentration of 100 nM. CPRs were injected into the sample cell at a concentration of 1.5 µg ml^{-1}. The injection volume was 50 µl, with 2 µl per injection (25 injections in total) at an injection interval of 300 s. The equilibrium time before the first injection was 600 s at 25 °C. The stirring rate was maintained at 300 r.p.m. during the course of measurements. The affinity constants were calculated with NanoAnalyze software (TA Instruments) with algorithms built into the software to analyse the data and to model the system with a constant blank model and an independent model.

LC–MS measurements. LC–MS was performed with a Waters system. Samples of 0.3 µl were aspirated using an autosampler and bound to a C18 capture column (5 µm, 5 × 0.3 mm), and then eluted into an analytical column (2.1 × 150 mm 1.7 µm) for separation. A 12 min analytical gradient (0 min of 2% B, 5 min of 10% B, 8 min of 30% B, 40% B for 10 min, and 12 min of 80% B, where A represents the stationary phase, and B represents the mobile phase) was established. The flow rate of the liquid phase was set to 0.3 ml min^{-1}. In positive-ion electrospray ionization MS mode analysis, each scan cycle included a full MS scan (m/z range, 20–1,500; ion accumulation time, 250 ms) and 40 subsequent MS/MS scans (m/z range, 100–1,500, ion accumulation time, 50 ms). The MS/MS acquisition conditions were set to a precursor ion signal greater than 120 c.p.s. and a charge number of +1 to +10. The ion repeat acquisition exclusion time was set to 18 s.

Experimental plant materials and cultured conditions. The tested tobacco variety *N. benthamiana* was the host of systemic infection of TMV (GFP-TMV), and *N. tabacum* cv. Samsun^{NN} was the host of dead spots of TMV. The experimental plants were cultured in an artificial climate chamber (25 °C temperature, 60% relative humidity, 2,000 lux illuminance and 16 h/8 h photoperiod; Shanghai Yiheng Scientific Instrument). The TMV was purified from the dead spots of *Nicotiana glutinosa* and bred on *N. tabacum* (NC89). The invasive clone of TMV-GFP was donated by Professor Jinguang Yang (Tobacco Research Institution of CAAS, PRC). Data are presented as mean ± s.d. (n = 5) and certain outlier plants were excluded from the experiments.

Extraction protocol for the tobacco protoplast. Four sterile tobacco seedlings (8 weeks old, 20 g) were collected and the main leaf veins and leaf tip tissues were removed; these parts were then cut with a scalpel blade into uniform filaments of 1–2 cm and transferred to a cell culture dish (10 cm × 10 cm). Next, the filaments were mixed with the enzymatic hydrolysis solution (15 ml) for 3 h on a horizontal constant temperature shaker in the dark (26 °C, 45 r.p.m.). The precooled W5 solution (4 °C, 15 ml) was added into this mixture and then filtered (200 mesh) into a sterile centrifuge tube (50 ml). After that, the collected solution was centrifuged twice to obtain pure protoplasts (25 °C, 1,400 r.p.m., 1 min, acceleration and elevation are 3; Eppendorf 5810R centrifuge). The pure protoplasts were resuspended in W5 solution (10 ml) and the intact protoplasts were settled in an ice bath for 1 h, then the supernatant was removed, and the intact protoplasts were stored in the MMg solution (10 ml) at 4 °C for subsequent experiments.

Enzymatic hydrolysis solution preparation: 0.28 g of cellulase (Shanghai Biological Technology Development), 0.048 g of macerozyme (Shanghai Biological Technology Development), mannitol (0.4 M), KCl (0.02 M) and morph ethyl sulfonic acid (MES) (0.02 M) were dissolved into sterile water (15 ml) under 55 °C for 10 min and then 0 °C for 10 min. Then, $CaCl_2$ (0.01 M), β-mercaptoethanol (0.005 M) and BSA (0.1% w/v) were added into the aforementioned mixture, filtered with a 0.45 µm filter membrane and then stored at 4 °C.

W5 solution preparation: NaCl (154 mM), $CaCl_2$ (125 mM), KCl (5 mM) and MES (2 mM) were dissolved into sterile water (500 ml). The solution was filtered with a 0.45 µm filter membrane before use.

MMg solution preparation: mannitol (400 mM), $MgCl_2$ (15 mM) and MES (4 mM) were dissolved into sterile water (500 ml). The solution was filtered with a 0.45 µm filter membrane before use.

Protoplast viability assessment. The viability of protoplasts was detected using the fluorescein diacetate (FDA) staining method[65]. Specifically, FDA could be hydrolysed into luciferin by esterase when it penetrated the protoplast membrane, whereas the luciferin could not penetrate the cell membrane[65]. Hence, the FDA staining method has frequently been used to assess the viability of protoplasts. For example, the extracted pure protoplasts (1 ml, 6.0×10^6) were incubated with FDA (2 µM) for 4 h (dark, 25 °C). Then, protoplasts were centrifuged twice for confocal imaging (1,400 r.p.m., 1 min; excitation wavelength of FDA, 488 nm).

The viability of protoplasts treated with different conditions was evaluated. Protoplasts were seeded in Petri dishes (the protoplast was divided into five dishes, named groups 1, 2, 3, 4 and 5; 500 µl, 10^6 per dish) and incubated in MMg solution at 25 °C. Group 1 was the control; group 2 was treated with 532 nm laser for 30 min and groups 3–5 were incubated with concentrations of 0.05, 0.5 and 5 mM, respectively, of chiral NPs (note that the concentration of copper is used here to represent different concentrations of chiral NPs) for 12 h. The FDA staining was assessed with a Leica TCS SP8 confocal fluorescence microscope (Leica Microsystems) and used to determine the viability of protoplasts.

Light-assisted cutting virus in protoplast extracted from infected *N. tabacum* cv. K326. The protoplasts (10^6 protoplasts per dish) were divided into eight groups and then the chiral NPs (5, 10 and 20 µM, respectively) were added into protoplasts and cocultured for 24 h. After 24 h, excess chiral NPs were removed through centrifugation (1,000 r.p.m., 1 min). The different dishes were illuminated with simulated sunlight for different times (4, 8 and 12 h). The antivirus was determined using laser scanning confocal microscopy (Leica).

RT–PCR. The leaves of infected *N. benthamiana* were collected and transferred into liquid nitrogen immediately to extract RNA according to the manual

of the total RNA Isolation Kit (Vazyme). TMV RNA was quantified with FastStart Universal SYBR Green Master. The primer pairs used for qPCR are GAGTAGACGACGCAACGG, CCAGAGGTCCAAACCAAAC for CPRs and CAAGGAAATCACCGCTTTGG, AAGGGATGCGAGGATGGA for actin, respectively. The $2^{-\Delta\Delta Q}$ method was used to calculate the expression of the target gene relative to that of the β-actin gene[66]. PCR data were obtained with a 7900HT fast real-time PCR system (Applied Biosystems).

Western blot analysis. The leaves of infected *N. tabacum* cv. Samsun^{NN} subjected to different treatments were collected and powdered under liquid nitrogen. The CPRs were extracted with a Plant Protein Extraction Kit (CoWin Biosciences). After separation by SDS–PAGE, the protein was transferred onto a polyvinylidenedifluoride (PVDF) membrane and allowed to partially dry. The protein sample was blocked with defatted milk powder in Tris-buffered saline plus Tween 20 (TBST) at 25 °C for 2 h and washed three times with TBST. The anti-TMV (1/2,000) or β-actin (1/5,000) antibody were incubated overnight with PVDF membrane at 4 °C. After washing three times with TBST, the membrane was incubated with a horseradish-peroxidase-conjugated secondary antibody (1/10,000). A chemiluminescence chromogenic kit reagent was added to the PVDF membrane for imaging.

Extraction protocol for TMV. Fresh, infected leaves from *N. tabacum* cv. K326 were selected and powdered under liquid nitrogen. The mixture was shaken for 1 min, after which the powder (20 mg) was mixed with 1 ml PBS (0.1 M, pH 7.2, containing 1% mercaptoethanol), and the mixture filtered with filter paper. Then, *n*-butanol (50 µl) was added to the filtrate, and the mixture was centrifuged (10,000 r.p.m., 15 min, 4 °C). The supernatant was collected and polyethylene glycol 3000 and NaCl were added to final concentrations of 4% (w/v) and 3% (w/v), respectively. The mixture was centrifuged at 4 °C, 10,000 r.p.m. for 15 min to obtain a precipitate, and then dissolved into PBS (0.01 M, pH 7.4) for use.

Light-assisted cutting virus in *N. benthamiana*. The *N. benthamiana* plants were randomly divided into four groups (G1–4; three plants per group), and then inoculated with the GFP-labelled TMV (8×10^8 c.f.u.) via the *Agrobacterium* into two leaves (two inoculation sites per leaf) in each of groups G1, G2 and G3. After culturing for 24 h, 5 µM of chiral NPs (total copper content) was sprayed onto each inoculated leaf in group G3 (5 ml per leaf), whereas groups G1 and G2 were treated with water and simulated sunlight, respectively. Group G4 was sprayed with chiral NPs and after 24 h the *Agrobacterium* were inoculated onto the corresponding leaves and cultured under simulated sunlight. The GFP fluorescence was monitored at days 3, 5 and 7.

Light-assisted virucidal activity *in N. tabacum* cv. Samsun^{NN}. Three healthy leaves from *N. tabacum* cv. Samsun^{NN} plants were randomly divided into three groups (control group, experiment group 1 and experiment group 2; one leaf per group), and then the TMV (1×10^8 c.f.u.) was inoculated through friction. After culturing for 24 h, the chiral NPs were sprayed onto each inoculated leaf in experiment group 1 and experiment group 2 at doses of 5 ml (1 µM, total copper content) and 5 ml (5 µM, total copper content), respectively, whereas the control group was treated with water. The number of dead spots was compared in the different treatment groups after 3 days.

Statistics and reproducibility. All the experimental data are presented as mean ± s.d. ($n=3$) with error bars representing the s.d. Significant differences were assessed by Student's *t*-test, with criteria of $^*P<0.05$, $^{**}P<0.01$, $^{***}P<0.001$, respectively. All the experimentally obtained micrographs shown in the main text and the Supplementary Information were representative experimental results from more than three independent experiments (at least $n=3$); the results of these independent experiments were highly consistent.

Reporting summary. Further information on research design is available in the Nature Research Reporting Summary linked to this article.

Data availability

The data that support the findings of this study are available from the corresponding authors upon reasonable request. The simulation data of the optimized models of Fig. 4 and the raw data of Table 2 are provided at https://doi.org/10.6084/m9.figshare.20045621. Source data are provided with this paper.

Received: 23 July 2021; Accepted: 5 July 2022;
Published online: 19 August 2022

References

1. Kah, M., Tufenkji, N. & White, J. C. Nano-enabled strategies to enhance crop nutrition and protection. *Nat. Nanotechnol.* **14**, 532–540 (2019).
2. He, S. & Creasey Krainer, K. M. Pandemics of people and plants: which is the greater threat to food security? *Mol. Plant* **13**, 933–934 (2020).
3. Jiang, G. et al. A rice NBS-ARC gene conferring quantitative resistance to bacterial blight is regulated by a pathogen effector-inducible miRNA. *Mol. Plant* **13**, 1752–1767 (2020).
4. Vriet, C., Russinova, E. & Reuzeau, C. Boosting crop yields with plant steroids. *Plant Cell* **24**, 842–857 (2012).
5. Hofmann, T. et al. Technology readiness and overcoming barriers to sustainably implement nanotechnology-enabled plant agriculture. *Nat. Food* **1**, 416–425 (2020).
6. Manfrin, A., Hanggli, A., van den Wildenberg, J. & McNeill, K. Substituent effects on the direct photolysis of benzotrifluoride derivatives. *Environ. Sci. Technol.* **54**, 11109–11117 (2020).
7. Yuan, X. et al. Frequent gain and loss of resistance against tobacco mosaic virus in *Nicotiana* species. *Mol. Plant* **8**, 1813–1815 (2015).
8. Pumplin, N. & Voinnet, O. RNA silencing suppression by plant pathogens: defence, counter-defence and counter-counter-defence. *Nat. Rev. Microbiol.* **11**, 745–760 (2013).
9. Zhu, H., Li, C. & Gao, C. Applications of CRISPR-Cas in agriculture and plant biotechnology. *Nat. Rev. Mol. Cell Biol.* **21**, 661–677 (2020).
10. Demirer, G. S. et al. Nanotechnology to advance CRISPR-Cas genetic engineering of plants. *Nat. Nanotechnol.* **16**, 243–250 (2021).
11. Giraldo, J. P., Wu, H., Newkirk, G. M. & Kruss, S. Nanobiotechnology approaches for engineering smart plant sensors. *Nat. Nanotechnol.* **14**, 541–553 (2019).
12. Lv, X. et al. Inhibitory effect of silver nanomaterials on transmissible virus-induced host cell infections. *Biomaterials* **35**, 4195–4203 (2014).
13. Chariou, P. L. et al. Soil mobility of synthetic and virus-based model nanopesticides. *Nat. Nanotechnol.* **14**, 712–718 (2019).
14. Jones, S. T. et al. Modified cyclodextrins as broad-spectrum antivirals. *Sci. Adv.* **6**, eaax9318 (2020).
15. Bowman, M. C. et al. Inhibition of HIV fusion with multivalent gold nanoparticles. *J. Am. Chem. Soc.* **130**, 6896–6897 (2008).
16. Kong, B. et al. Virucidal nano-perforator of viral membrane trapping viral RNAs in the endosome. *Nat. Commun.* **10**, 185 (2019).
17. Wang, W. et al. Dual-targeting nanoparticle vaccine elicits a therapeutic antibody response against chronic hepatitis B. *Nat. Nanotechnol.* **15**, 406–416 (2020).
18. Mitter, N. et al. Clay nanosheets for topical delivery of RNAi for sustained protection against plant viruses. *Nat. Plants* **3**, 16207 (2017).
19. Torney, F., Trewyn, B. G., Lin, V. S. & Wang, K. Mesoporous silica nanoparticles deliver DNA and chemicals into plants. *Nat. Nanotechnol.* **2**, 295–300 (2007).
20. Chung, Y. H., Beiss, V., Fiering, S. N. & Steinmetz, N. F. COVID-19 vaccine frontrunners and their nanotechnology design. *ACS Nano* **14**, 12522–12537 (2020).
21. Chariou, P. L. & Steinmetz, N. F. Delivery of pesticides to plant parasitic nematodes using tobacco mild green mosaic virus as a nanocarrier. *ACS Nano* **11**, 4719–4730 (2017).
22. Yang, T. & Duncan, T. V. Challenges and potential solutions for nanosensors intended for use with foods. *Nat. Nanotechnol.* **16**, 251–265 (2021).
23. Kotov, N. A. Chemistry. Inorganic nanoparticles as protein mimics. *Science* **330**, 188–189 (2010).
24. Lauster, D. et al. Phage capsid nanoparticles with defined ligand arrangement block influenza virus entry. *Nat. Nanotechnol.* **15**, 373–379 (2020).
25. Kwon, P. S. et al. Designer DNA architecture offers precise and multivalent spatial pattern-recognition for viral sensing and inhibition. *Nat. Chem.* **12**, 26–35 (2020).
26. Vigant, F., Santos, N. C. & Lee, B. Broad-spectrum antivirals against viral fusion. *Nat. Rev. Microbiol.* **13**, 426–437 (2015).
27. Cagno, V. et al. Broad-spectrum non-toxic antiviral nanoparticles with a virucidal inhibition mechanism. *Nat. Mater.* **17**, 195–203 (2018).
28. Xu, L. et al. Enantiomer-dependent immunological response to chiral nanoparticles. *Nature* **601**, 366–373 (2022).
29. Dong, J. et al. Free-standing homochiral 2D monolayers by exfoliation of molecular crystals. *Nature* **602**, 606–611 (2022).
30. Yan, J. et al. Self-assembly of chiral nanoparticles into semiconductor helices with tunable near-infrared optical activity. *Chem. Mater.* **32**, 476–488 (2019).
31. Yang, M. et al. Self-assembly of nanoparticles into biomimetic capsid-like nanoshells. *Nat. Chem.* **9**, 287–294 (2017).
32. Zhang, Q. et al. Unraveling the origin of chirality from plasmonic nanoparticle-protein complexes. *Science* **365**, 1475–1478 (2019).
33. Sun, M. et al. Site-selective photoinduced cleavage and profiling of DNA by chiral semiconductor nanoparticles. *Nat. Chem.* **10**, 821–830 (2018).
34. Hou, K. et al. Chiral gold nanoparticles enantioselectively rescue memory deficits in a mouse model of Alzheimer's disease. *Nat. Commun.* **11**, 4790 (2020).
35. Ge, P. & Zhou, Z. H. Hydrogen-bonding networks and RNA bases revealed by cryo electron microscopy suggest a triggering mechanism for calcium switches. *Proc. Natl Acad. Sci. USA* **108**, 9637–9642 (2011).

36. Zhang, H., Zhao, J., Liu, S., Zhang, D. P. & Liu, Y. Tm-22 confers different resistance responses against tobacco mosaic virus dependent on its expression level. *Mol. Plant* **6**, 971–974 (2013).
37. Ge, P. & Zhou, Z. H. Hydrogen-bonding networks and RNA bases revealed by cryo electron microscopy suggest a triggering mechanism for calcium switches. *Proc. Natl Acad. Sci. USA* **108**, 9637–9642 (2011).
38. Kim, J. Y. et al. Assembly of gold nanoparticles into chiral superstructures driven by circularly polarized light. *J. Am. Chem. Soc.* **141**, 11739–11744 (2019).
39. Qu, A. et al. Stimulation of neural stem cell differentiation by circularly polarized light transduced by chiral nanoassemblies. *Nat. Biomed. Eng.* **5**, 103–113 (2021).
40. Yeom, J. et al. Chiromagnetic nanoparticles and gels. *Science* **359**, 309–314 (2018).
41. Moloney, M. P., Gun'ko, Y. K. & Kelly, J. M. Chiral highly luminescent CdS quantum dots. *Chem. Commun. (Camb.)* **38**, 3900–3902 (2007).
42. Sperling, R. A., Rivera Gil, P., Zhang, F., Zanella, M. & Parak, W. J. Biological applications of gold nanoparticles. *Chem. Soc. Rev.* **37**, 1896–1908 (2008).
43. Liu, J. et al. Luminescent gold nanoparticles with size-independent emission. *Angew. Chem. Int. Ed.* **55**, 8894–8898 (2016).
44. Sharma, P., Jha, A. B., Dubey, R. S. & Pessarakli, M. Reactive oxygen species, oxidative damage, and antioxidative defense mechanism in plants under stressful conditions. *J. Bot.* **2012**, 1–26 (2012).
45. Yin, J. J. et al. Phototoxicity of nano titanium dioxides in HaCaT keratinocytes—generation of reactive oxygen species and cell damage. *Toxicol. Appl. Pharmacol.* **263**, 81–88 (2012).
46. Pospisil, P. Production of reactive oxygen species by photosystem II as a response to light and temperature stress. *Front Plant Sci.* **7**, 1950–1962 (2016).
47. Jones, B. J., Vergne, M. J., Bunk, D. M., Locascio, L. E. & Hayes, M. A. Cleavage of peptides and proteins using light-generated radicals from titanium dioxide. *Anal. Chem.* **79**, 1327–1332 (2007).
48. Ludwig, J. et al. Ultrafast hole trapping and relaxation dynamics in p-type CuS nanodisks. *J. Phys. Chem. Lett.* **6**, 2671–2675 (2015).
49. Gilmanshin, R., Williams, S., Callender, R. H., Woodruff, W. H. & Dyer, R. B. Fast events in protein folding: relaxation dynamics of secondary and tertiary structure in native apomyoglobin. *Proc. Natl Acad. Sci. USA* **94**, 3709–3713 (1997).
50. Dolan, E. A., Yelle, R. B., Beck, B. W., Fischer, J. T. & Ichiye, T. Protein control of electron transfer rates via polarization: molecular dynamics studies of rubredoxin. *Biophys. J.* **86**, 2030–2036 (2004).
51. Li, L., Li, C., Zhang, Z. & Alexov, E. On the dielectric "constant" of proteins: smooth dielectric function for macromolecular modeling and its implementation in DelPhi. *J. Chem. Theory Comput.* **9**, 2126–2136 (2013).
52. Amin, M. & Kupper, J. Variations in proteins dielectric constants. *ChemistryOpen* **9**, 691–694 (2020).
53. Ly, H. G. T. et al. Superactivity of MOF-808 toward peptide bond hydrolysis. *J. Am. Chem. Soc.* **140**, 6325–6335 (2018).
54. El-Shetehy, M. et al. Silica nanoparticles enhance disease resistance in *Arabidopsis* plants. *Nat. Nanotechnol.* **16**, 344–353 (2021).
55. Hu, P. et al. Nanoparticle charge and size control foliar delivery efficiency to plant cells and organelles. *ACS Nano* **14**, 7970–7986 (2020).
56. Guo, W., Lu, X., Liu, B., Yan, H. & Feng, J. Anti-TMV activity and mode of action of three alkaloids isolated from *Chelidonium majus*. *Pest Manag Sci.* **77**, 510–517 (2021).
57. Adeel, M. et al. Carbon-based nanomaterials suppress tobacco mosaic virus (TMV) infection and induce resistance in *Nicotiana benthamiana*. *J. Hazard. Mater.* **404**, 124167 (2021).
58. Gilbertson, L. M. et al. Guiding the design space for nanotechnology to advance sustainable crop production. *Nat. Nanotechnol.* **15**, 801–810 (2020).
59. Kah, M., Kookana, R. S., Gogos, A. & Bucheli, T. D. A critical evaluation of nanopesticides and nanofertilizers against their conventional analogues. *Nat. Nanotechnol.* **13**, 677–684 (2018).
60. Wang, L. et al. Arabinogalactan protein–rare earth element complexes activate plant endocytosis. *Proc. Natl Acad. Sci. USA* **116**, 14349–14357 (2019).
61. Wong, M. H. et al. Nitroaromatic detection and infrared communication from wild-type plants using plant nanobionics. *Nat. Mater.* **16**, 264–272 (2017).
62. Dousset, S. et al. Facilitated transport of diuron and glyphosate in high copper vineyard soils. *Environ. Sci. Technol.* **41**, 8056–8061 (2007).
63. Ma, G. X. et al. Self-assembly of copper sulfide nanoparticles into nanoribbons with continuous crystallinity. *ACS Nano* **7**, 9010–9018 (2013).
64. Zhang, J., Zhou, K., Zhang, Y., Du, M. & Wang, Q. Precise self-assembly of nanoparticles into ordered nanoarchitectures directed by tobacco mosaic virus coat protein. *Adv. Mater.* **31**, e1901485 (2019).
65. King, M. A. Detection of dead cells and measurement of cell killing by flow cytometry. *J. Immunol. Methods* **243**, 155–166 (2000).
66. Gan, H. et al. Dynamics of 5-hydroxymethylcytosine during mouse spermatogenesis. *Nat. Commun.* **4**, 1995 (2013).

Acknowledgements

This work is financially supported by the National Key R&D Program (2021YFA1200300), and is also supported by the National Natural Science Foundation of China (32071400, 21925402, 21977038). N.A.K is grateful to NSF 1463474 and NSF 1566460 for support. We are grateful to the Brazilian funding agencies CAPES (Finance Code 001), CNPq (process 311353/2019-3) and FAPESP (processes 2012/15147-4 and 2013/07296-2) for financial support and the HPC resources provided by the SDumont supercomputer at the National Laboratory for Scientific Computing (LNCC/MCTI, Brazil, http://sdumont.lncc.br) and by the Cloud@UFSCar.

Author contributions

H.K., N.A.K. and C.X. conceived the project and designed the experiments. J.Y. was responsible for the antiviral experiments on tobacco and plant cells. R.G. was responsible for the synthesis and characterization of the chiral NPs and studied their photoinduced cleavage properties. R.G., L.X. and M.S. carried out the CD, western blot, XPS, X-ray diffraction, LC–MS–MS and ROS experiments. M.X. performed the test on antiviral activity in TMV plants. C.H. and X.G. helped to synthesis, characterize and analyse the mechanism. F.M.C., X.Z., P.K. and A.F.M. performed the MD, QM and DFT simulations, and analysed the results. H.K. and N.A.K. conceptualized the work. C.X. supervised the study. H.K., N.A.K. and C.X. analysed and discussed the results and wrote the manuscript

Competing interests

The authors declare no competing interests.

Additional information

Supplementary information The online version contains supplementary material available at https://doi.org/10.1038/s41929-022-00823-1.

Correspondence and requests for materials should be addressed to Chuanlai Xu, Jinguang Yang, Nicholas A. Kotov or Hua Kuang.

Peer review information *Nature Catalysis* thanks Fabienne Schwab, Lixia Zhao, Vladimir Lobaskin and the other, anonymous, reviewer(s) for their contribution to the peer review of this work.

Reprints and permissions information is available at www.nature.com/reprints.

Publisher's note Springer Nature remains neutral with regard to jurisdictional claims in published maps and institutional affiliations.

nature portfolio

Corresponding author(s): Chuanlai Xu, Jinguang Yang, Nicholas A. Kotov, Hua Kuang

Last updated by author(s): Jun 15, 2022

Reporting Summary

Nature Portfolio wishes to improve the reproducibility of the work that we publish. This form provides structure for consistency and transparency in reporting. For further information on Nature Portfolio policies, see our Editorial Policies and the Editorial Policy Checklist.

Statistics

For all statistical analyses, confirm that the following items are present in the figure legend, table legend, main text, or Methods section.

n/a	Confirmed	
☐	☒	The exact sample size (*n*) for each experimental group/condition, given as a discrete number and unit of measurement
☐	☒	A statement on whether measurements were taken from distinct samples or whether the same sample was measured repeatedly
☐	☒	The statistical test(s) used AND whether they are one- or two-sided *Only common tests should be described solely by name; describe more complex techniques in the Methods section.*
☐	☒	A description of all covariates tested
☐	☒	A description of any assumptions or corrections, such as tests of normality and adjustment for multiple comparisons
☐	☒	A full description of the statistical parameters including central tendency (e.g. means) or other basic estimates (e.g. regression coefficient) AND variation (e.g. standard deviation) or associated estimates of uncertainty (e.g. confidence intervals)
☒	☐	For null hypothesis testing, the test statistic (e.g. *F*, *t*, *r*) with confidence intervals, effect sizes, degrees of freedom and *P* value noted *Give P values as exact values whenever suitable.*
☒	☐	For Bayesian analysis, information on the choice of priors and Markov chain Monte Carlo settings
☒	☐	For hierarchical and complex designs, identification of the appropriate level for tests and full reporting of outcomes
☒	☐	Estimates of effect sizes (e.g. Cohen's *d*, Pearson's *r*), indicating how they were calculated

Our web collection on statistics for biologists contains articles on many of the points above.

Software and code

Policy information about availability of computer code

Data collection	Gatan Microscopy Suite Software, Lieca LAS AF Lite, Imaging Lab, Chirascan,ITC run, jade6, MassLynx V4.1, Zetasizer Software, Omnic, iBright 1500
Data analysis	OriginPro 8.5, NanoAnalyze

For manuscripts utilizing custom algorithms or software that are central to the research but not yet described in published literature, software must be made available to editors and reviewers. We strongly encourage code deposition in a community repository (e.g. GitHub). See the Nature Portfolio guidelines for submitting code & software for further information.

Data

Policy information about availability of data

All manuscripts must include a data availability statement. This statement should provide the following information, where applicable:

- Accession codes, unique identifiers, or web links for publicly available datasets
- A description of any restrictions on data availability
- For clinical datasets or third party data, please ensure that the statement adheres to our policy

The data supporting the findings of this study are available within the paper and its Supplementary Information files and are available from the corresponding author upon reasonable request.

Field-specific reporting

Please select the one below that is the best fit for your research. If you are not sure, read the appropriate sections before making your selection.

☒ Life sciences ☐ Behavioural & social sciences ☐ Ecological, evolutionary & environmental sciences

For a reference copy of the document with all sections, see nature.com/documents/nr-reporting-summary-flat.pdf

Life sciences study design

All studies must disclose on these points even when the disclosure is negative.

Sample size	All the experiments were performed in at least three replicates. Sample sizes for experiments were estimated based on previous experience with a similar studies. Statistical analysis was carried out with at least 3 independent samples. Experiments involving plants were carried out in groups. A total of 4 groups with 3 plants each were used. The experiments for each group were performed in three replicates.
Data exclusions	No data was excluded from the analyses.
Replication	For each experiment and condition, at least three independent technical replicates were performed. All observations reported in the manuscript were reproducible.
Randomization	The plant applied in this experiment were randomly selected and divided into different groups, each group contained 3 plants.
Blinding	The investigators were blinded to group allocation during data collection and/or analysis. All samples were analyzed using the reported approach without prior knowledge of the level of exposure.

Reporting for specific materials, systems and methods

We require information from authors about some types of materials, experimental systems and methods used in many studies. Here, indicate whether each material, system or method listed is relevant to your study. If you are not sure if a list item applies to your research, read the appropriate section before selecting a response.

Materials & experimental systems

n/a	Involved in the study
☐	☒ Antibodies
☒	☐ Eukaryotic cell lines
☒	☐ Palaeontology and archaeology
☒	☐ Animals and other organisms
☒	☐ Human research participants
☒	☐ Clinical data
☒	☐ Dual use research of concern

Methods

n/a	Involved in the study
☒	☐ ChIP-seq
☒	☐ Flow cytometry
☒	☐ MRI-based neuroimaging

Antibodies

Antibodies used	The anti-TMV antibody was purchased from Agdia Inc (SRA57400, Elkhart), USA. Rabbit anti GFP-Tag mAb was purchased from ABclonal (AE078)
Validation	anti-TMV antibody (Species Reactivity: Tobamovirus species; Application: ELISA, WB); Rabbit anti GFP-Tag mAb (Species Reactivity: Recombinant protein GFP protein; Application: IF, WB)